Ocean and Coastal Management 245 (2023) 106871

Contents lists available at ScienceDirect

Ocean and Coastal Management

journal homepage: www.elsevier.com/locate/ocecoaman

Improvements in the design of nest cavities to attract cephalopods and crustaceans in a green artificial reef unit according to tridimensional hydrodynamic criteria – Application to the Ares-Betanzos estuary

Luis Carral [a,*], María Isabel Lamas [a], Mateo Fouz [b], Iván López [b], Rodrigo Carballo [b]

[a] Escola Politécnica de Enxeñaría de Ferrol (EPEF), Campus Industrial de Ferrol, Universidade da Coruña, Rúa Mendizabal s/n, 15403, Ferrol, Spain
[b] Escola Politécnica Superior de Enxeñaría (EPSE), Departamento de Enxeñaría Agroforestal, Universidade de Santiago de Compostela, Rúa Benigno Ledo s/n, 27002, Lugo, Spain

ARTICLE INFO

Keywords:
Artificial reef
Estuary
Currents
CFD
Numerical modelling

ABSTRACT

Installing artificial reefs (ARs) on the seabed creates a hard substrate that alters water flow and causes different species to settle. For this reason, by applying hydrodynamics to ARs, a useful tool is created for analysing these reefs so that there is adequate nutrient circulation and a propitious habitat for benthic and pelagic fauna. Using hydrodynamic criteria to characterise the velocity field, the present work aims to propose a methodology for positioning nest cavities within an AR unit in which different species will settle. Biological considerations, such as nutrient supply as well as the most suitable size and shape for the nest cavities, are taken into account. A state-of-the-art 3D shallow water model is validated and applied to the Ares-Betanzos estuary (NW Spain), where the installation of an AR group has recently been proposed. This coastal body, with a complex 3D hydrodynamic structure, was achieved under representative average conditions in absence of winds, which in turn greatly differs both in space and time throughout a spring-neap tidal cycle. A 3D CFD (Computational Fluid Dynamics) tool is applied to model food delivery on the AR. Moreover, the optimal geometry and position of nest cavities are established through a created indicator, $AR_{nest\ cavity\ position}$, in order to provide sufficient nutrient circulation. It was found that the most appropriate shape for the nest cavities is cylindrical and a diameter of 200–300 mm is the most appropriate size. In terms of the ideal positions for the nest cavities, these depend on the orientation of the AR with respect to the current velocity. One of the orientations analysed leads to sufficient nutrient supply to the whole AR, while the other orientation analysed leads to sufficient nutrient supply to the high and mid positions at the front face, mid and low positions at the back face and all positions along the lateral faces.

1. Introduction

Marine ecosystems are seriously threatened around the world due to global warming, water pollution and unsustainable fishing patterns (Lotze et al., 2018). Many coastal habitats are reaching the global limit of impact absorption due to the great pressures they face. This issue has repercussions on the quality of the underwater life, which is being harmed to a great degree. Furthermore, this damage is continuously increasing; oceans will soon face overexploitation unless extractive activities and the general economic activity which pollute ecosystems are regulated according to sustainability criteria (Rickels et al., 2016). A further factor is that many coastal zones are subjected to a high impact of recreational activities, aquaculture and artisanal fishing.

Managing coastal ecosystems, especially in relation to aquaculture and artisanal fishing, is a major concern for society (Bacher et al., 2003). In the region of Galicia (NW Spain), this issue is crucial: its coastal regions, especially its estuaries, stand out due to their unique characteristics and environmental, economic and social factors (Carral et al., 2018).

AR groups are made up of a set of AR units. Arranged in an orderly fashion on the seabed, these units perform the functions of natural reef systems, *i.e.*, concentrate and improve the population of living marine organisms (London Convention and Protocol/UNEP, 2009; Kim et al., 2016). These functions play a key role in the management of coastal zones. The structural complexity of habitats near reefs plays a crucial role in protecting biodiversity. In natural, complex marine ecosystems,

* Corresponding author.
E-mail address: l.carral@udc.es (L. Carral).

https://doi.org/10.1016/j.ocecoaman.2023.106871
Received 24 April 2023; Received in revised form 25 September 2023; Accepted 26 September 2023
Available online 9 October 2023

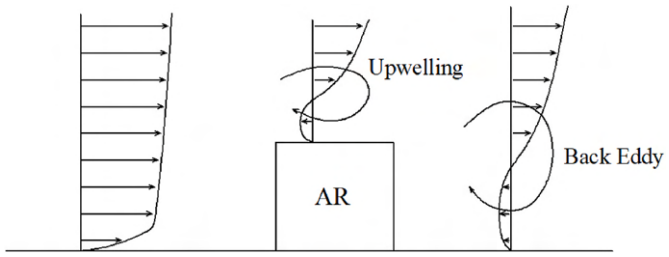

Fig. 1. Typical modification of the velocity profile around an artificial reef unit.

like rocky or coral reefs and mangroves, the presence of diverse microhabitats makes it possible for a wide range of species to coexist. These habitats provide shelter, food sources and breeding grounds for numerous marine organisms, including fish, invertebrates and plants. With ARs, a similar structural complexity is created to mimic the conditions found in natural ecosystems. The presence of ARs can enhance the overall biodiversity of an area by attracting a wide array of species; their enhanced structural complexity and habitat heterogeneity promote the richness and abundance of marine species. An increase in biodiversity associated with ARs has positive ecological consequences. Biodiversity enhances the stability and resilience of ecosystems, improves nutrient cycling and contributes to various ecological goods and services.

Despite these benefits, it is essential to consider the potential risks of ARs, especially pollution and the invasion of alien species. The materials used in ARs may include pollutants, which have a negative effect on ecosystems. Regarding invasions, ARs may facilitate the introduction of non-native organisms, which can outcompete or prey upon native species, disrupt ecosystems and alter biodiversity. To mitigate this risk, regular monitoring must take place to assess the environmental impacts of ARs.

From a hydrodynamic point of view, installing ARs on the seabed alters the water velocity field, promoting adequate nutrient circulation. The presence of the AR creates a basal effect through a vertical velocity gradient, as can be seen in Fig. 1. The water flow from the seabed is separated and directed upwards to create an upwelling. A back eddy is created at the back of the AR module. Both upwelling and back vortices move the water flow along the plane parallel to the current. At the same time, part of the water is displaced sideways. The upwelling vortex promotes a vertical circulation of the water (Wang et al., 2018), which increments the transport of nutrients from the seabed and improves their supply through the reef (Haro et al., 2004; Lan et al., 2004). The back part of the reef is critical. As this section is not directly exposed to the water current, the supply of nutrients is scarce in this region. Nevertheless, the back eddy considerably improves the circulation of nutrients at the back part. Many studies have highlighted that fish tend to group around ARs due to the favourable conditions created by the alteration in the velocity field (Bohnsack and Sutherland, 1985; Collins et al., 1990; Godoy et al., 2002).

The effects of the shape and structure of the ARs are a further challenge (Pickering and Whitmarsh, 1997). There is interest in cube-shaped ARs due to their simplicity and, therefore, cheaper manufacture (Carral et al., 2020; Wang et al., 2018). On the other hand, from a hydrodynamic point of view, cube-shapes favour the eddies illustrated in Fig. 1 (Carral et al., 2022).

Several experiments using wind tunnels and numerical simulations based on CFD (Computational Fluid Dynamics) have been carried out. In many of these studies, cubic shapes are used. Wang et al. (2018) have analysed the angle of the current velocity around ARs. Liu et al. (2012) found that cubic shapes present a low variation in the height and upwelling region with the current velocity. Using CFD and an experimental setup in a wind tunnel, Liu and Su (2013) analysed how the distribution of different AR units has an impact. Huang et al. (2014) performed numerical simulations to study the influence of the openings and current velocity in the velocity field of cubic reefs. Zheng et al. (2022) used PIV (Particle Image Velocimetry) and a numerical model to analyse how the AR configuration affects turbulence.

The present work focuses on ARs that are to be installed in the Ares-Betanzos estuary (NW Spain). Many species, both benthonic and pelagic, are common to this zone. The ARs aim to restore the production of cephalopods and crustaceans, the species that have experienced the most significant reduction in recent years. The main goal of this study is to develop a methodology for defining nest cavities inside the ARs units to be placed in the Ares-Betanzos estuary. To this end, the 3D hydrodynamics in the AR unit are characterised through state-of-the-art numerical modelling and by considering the major forcings: tides, water discharges and thermohaline conditions. On the bases of the 3D velocity field, the position of the nest cavities is determined in order to get sufficient nutrient circulation, as well as to validate the geometry of the AR unit according to biological criteria. To evaluate the effectiveness of the nutrient circulation, the velocity field around and inside the AR is employed. It is worth mentioning that the chosen cubic shape has the risk of seabed burial. The burial effect may be significant in soft seabeds, modifying the flow field around ARs (Yoon et al., 2016; Oudon et al., 2022) and reducing the useable volume (Yoon et al., 2016; Wang et al., 2018). Nevertheless, this effect is out of the scope of the present work and is proposed for future research. At the same time, stability aspects, such as rolling and slipping, are also proposed as future research projects.

2. Models, methods and results

The AR units proposed in the present work are shown in Fig. 2. These ARs are considered "green" given that sustainable alternative materials have been proposed in previous works (Carral et al., 2020; Camba et al., 2021; Carral et al., 2023). As these AR units will be transported by road trucks, they have been designed following logistic criteria: cubic structures with an edge of 1500 mm. The faces have nest cavities of 200 and 300 mm in diameter, taking into account the species that will colonise the AR. These dimensions will be justified in Section 2.3.1. An interior hole, 600 mm in diameter, connects the exterior with the interior in order to provide light, as well as a pathway for nutrient reception. Two lateral holes, 250 and 450 mm in diameter, also link the exterior to the

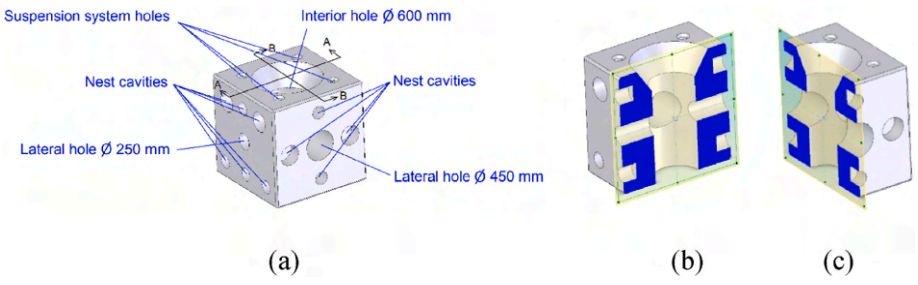

Fig. 2. Design of the artificial reef. (a) 3D; (b) AA section; (c) BB section.

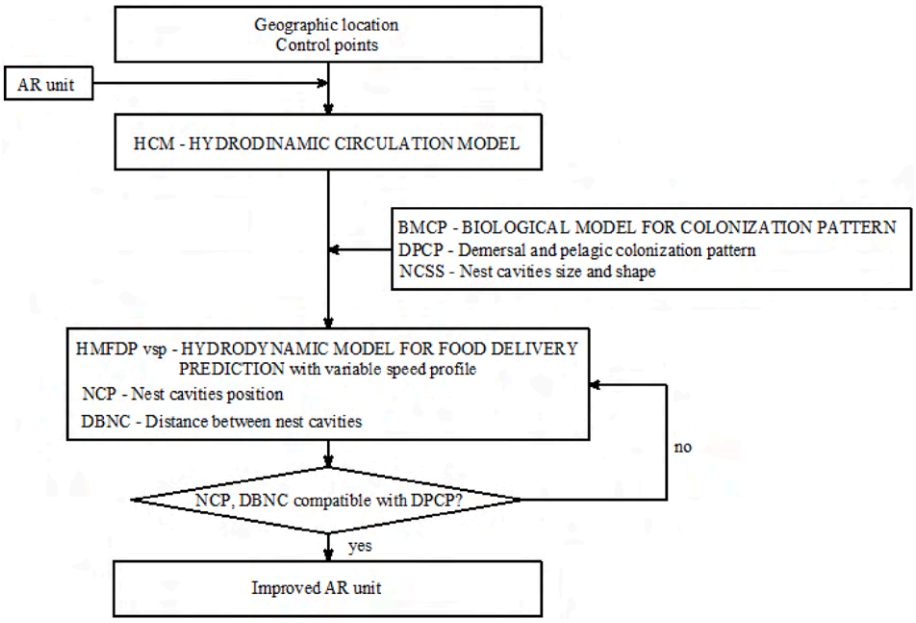

Fig. 3. Flowchart related to the methodology employed.

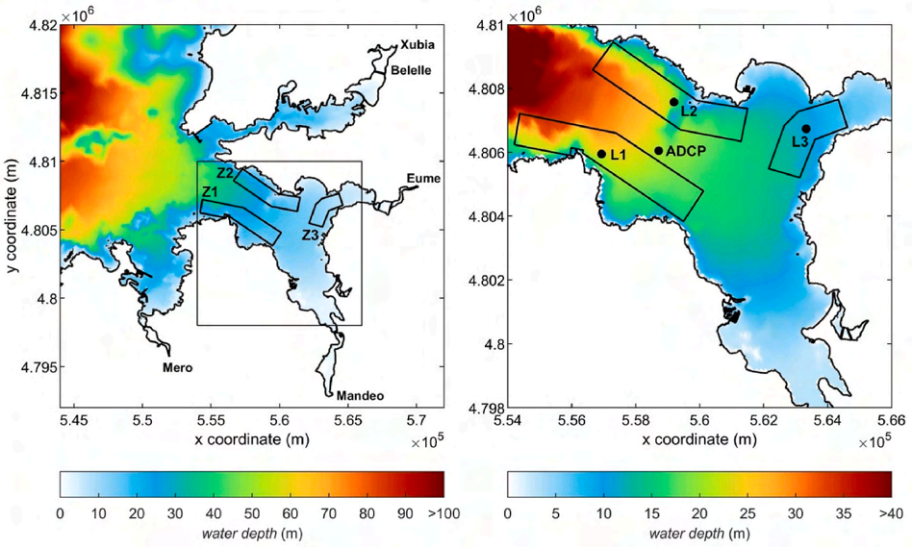

Fig. 4. Bathymetric configuration as interpolated to the numerical grid, pinpointing the main river discharges in the coastal region and the zones of interest (Z1, Z2, Z3) within the Ares-Betanzos estuary for AR deployment (general overview, left), along with their representative locations (L1, L2, L3) and the ADCP site (detail, right).

interior. These dimensions were selected according to previous hydrodynamic analyses (Carral et al., 2021) to guarantee circulation into the interior part of the AR and thus a continuous supply of nutrients. Moreover, small, vertical holes are made so that the unit can be installed in the sea. During installation, the AR is suspended through ropes, which are introduced into these suspension system holes.

The methodology adopted for the present work is summarised in Fig. 3. First of all, the most appropriate location to install AR units must be chosen. The present work focuses on Galicia. In a previous work, the Ares-Betanzos estuary was established as the most suitable location in Galicia (Carral et al., 2018). The analysis of the estuary entails developing a 3D hydrodynamic circulation model (HCM) to characterise the current velocity against depth on different control points. A biological model for colonisation pattern (BMCP) is created for this estuary. The demersal and pelagic colonisation pattern (DPCP) (Rodriguez-Guerreiro *et al.* 2019), is used to establish the ideal nest cavity shape and size (NCSS). Using these biological data and the current velocity profile, a model based on CFD is developed to analyse the hydrodynamic model for food delivery prediction (HMFDP). A variable speed profile (vsp) with the depth is considered, hence this delivery model's denomination, HMFDP vsp. This model predicts the velocity field inside and around the AR; it is used to determine the nest cavities positions (NCP) and distance between nest cavities (DBNC). The compatibility with the DPCP is checked, i.e., the hydrodynamic criteria must fulfil biological requirements in order to promote a suitable colonisation pattern. To summarise, the proposed methodology optimises the NCP and DBNC and maximises the number of cavities on each surface, all in accordance with biological requirements.

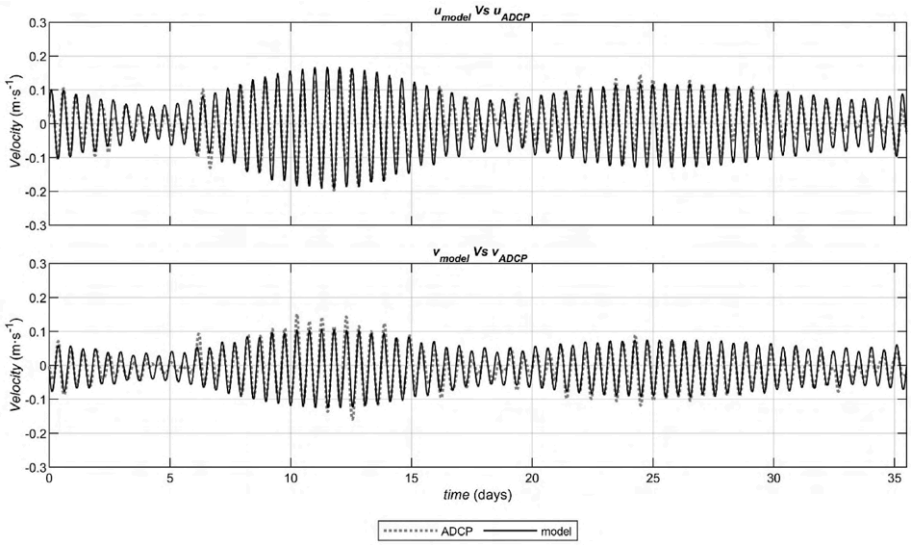

Fig. 5. Velocity in *x*-direction (above) and velocity in *y*-direction (below) registered by the ADCP (grey dots) and computed by the model (black, continuous line).

2.1. Hydrodynamic circulation model (HCM)

From the hydrodynamic point of view, two aspects must be taken into account in order to create a suitable habitat for allocating species in the AR.

i) The hydrodynamic pattern of a global coastal area.
ii) The fine detail of the hydrodynamic pattern in the much smaller region encompassed by the AR module.

As their spatial scales are different, both hydrodynamic models cannot be developed in the same simulation. For this reason, two models are produced in the present work. Therefore, the data from the hydrodynamic pattern of a global coastal area (HCM model), dealt with in Section 2.1, constitute the boundary conditions for the detailed hydrodynamic model applied to the region that encompasses the AR module (HMFDP model), explained in Section 2.2.

In this section, corresponding to the HCM model, a state-of-the-art 3D shallow water model is validated and applied to the Ares-Betanzos estuary. It has been found that this coastal body presents a complex 3D hydrodynamic structure under representative average conditions in the absence of winds, which in turn greatly differs both in space and time throughout a spring-neap tidal cycle. In order to address the 3D vertical structure at different locations identified to be of interest for AR operation, site-specific 3D velocity parameters are determined to be used as input for subsequent AR optimisation through CFD modelling in Section 2.2.

2.1.1. Numerical modelling implementation

AR group design should resort to an accurate hydrodynamic characterisation of the coastal area where they are intended to be deployed. In this regard, estuaries emerge as promising coastal areas for AR operation. These coastal areas usually present complex hydrodynamic patterns. This is primarily the case when the tide and other forcing factors, such as river discharges or wind action, play a key role in driving coastal circulation.

This factor is of particular interest in estuaries without large tidal ranges, which may result in complex 3D flow patterns present not only during specific events (*e. g.*, high river discharges or winds), but also during average conditions in the absence of winds (Carballo et al., 2009). This is the case of the Ares-Betanzos estuary, a mesotidal estuary during spring tides and microtidal during neap tides. Here, 3D patterns have been previously described, with river discharges generating a positive circulation irrespective of the local wind regime (Duarte et al., 2014), which in turn can be influenced under certain conditions by the hydrodynamics of the nearby A Coruña (to the W) and Ferrol (to the N) estuaries, Fig. 4. Thus, accurately characterising the presence of a 3D transient circulation structure, under average conditions considering representative periods of time, is of particular interest when AR groups are being designed. As these groups are deployed alongthe seabed, they are subsequently subject to bottom-layer flows.

The state-of-the-art open-source model Deltares (2010) is applied to this coastal area. It approximates Shallow Water equations, comprising the continuity equation for an incompressible fluid (Eq. (1)), and the momentum equations in *x*-direction, *y*-direction (Eq. (2)), and *z*-direction (Eq. (3)), the latter being simplified according to the shallow water assumption to the hydrostatic pressure distribution. In addition, to compute the horizontal density gradients and the resulting baroclinic flows, these equations are solved coupled to the transport equation (Eq. 4). These equations read:

$$\frac{\partial u}{\partial x}+\frac{\partial v}{\partial y}+\frac{\partial w}{\partial z}=M \tag{1}$$

$$\frac{Du}{Dt}=fv-g\frac{\partial \zeta}{\partial x}-\frac{g}{\rho_0}\int_{z=z}^{z=\zeta}\frac{\partial \rho}{\partial x}dz'+\upsilon_h\left(\frac{\partial^2 u}{\partial x^2}+\frac{\partial^2 u}{\partial y^2}\right)+\upsilon_v\left(\frac{\partial^2 u}{\partial z^2}\right)$$

$$\frac{Dv}{Dt}=-fu-g\frac{\partial \zeta}{\partial y}-\frac{g}{\rho_0}\int_{z=z}^{z=\zeta}\frac{\partial \rho}{\partial y}dz'+\upsilon_h\left(\frac{\partial^2 v}{\partial x^2}+\frac{\partial^2 v}{\partial y^2}\right)+\upsilon_v\left(\frac{\partial^2 v}{\partial z^2}\right) \tag{2}$$

$$\frac{\partial p}{\partial z}=-\rho g \tag{3}$$

$$\frac{Dc}{Dt}=D_h\left(\frac{\partial^2 c}{\partial x^2}+\frac{\partial^2 c}{\partial y^2}\right)+D_v\frac{\partial^2 c}{\partial z^2}-\lambda_d c+C \tag{4}$$

where, *u, v* and *w* are the components of the flow velocity in *x*-, *y*- and *z*-direction, respectively; ζ stands for the free surface displacement; ρ and ρ_0 represent the density and reference density of oceanic water, respectively; *M* accounts for the mass source term; *f* is the Coriolis parameter; υ_h and υ_v stand for the horizontal and vertical turbulent eddy viscosity, respectively; *c* represents either salinity or temperature constituents; D_h and D_v are the horizontal and vertical turbulent eddy diffusivity, respectively; λ_d represents decay processes of first order; finally, *C* stands for the salinity or temperature source term. The model is

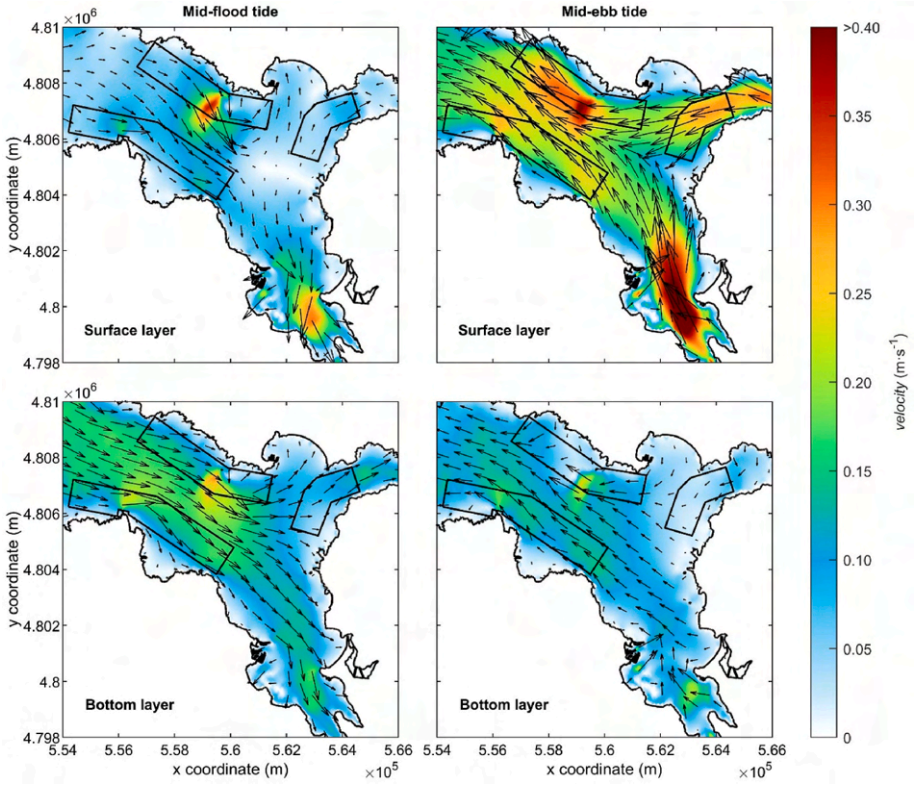

Fig. 6. Transient circulation during mid-flood (left) and mid-ebb tide (right) of a mean spring tide at surface (above) and bottom (below) layers.

applied with a spatial resolution of 100 m within the estuary, progressively increasing its size up to 250 m in the open ocean boundaries located at about a 25 km distance from the estuary's mouth, and covering the whole hydrodynamic system made up of the Ares-Betanzos, A Coruña and Ferrol estuaries, Fig. 4.

High-resolution bathymetry data are interpolated to the grid, Fig. 4, leading to solve the influence of the complex coastal configuration on hydrodynamics. Moreover, the vertical discretisation should accurately characterise the flow throughout the water column, and, in particular, close to the sea bottom, where the AR is to be deployed. To this end, a σ-grid representation is assumed. In this representation, the width of the vertical layers is set as a percentage of the local water depth, leading to a better vertical representation than the z-grid approach in the case of shallow coastal areas. A total of 12 layers are defined with resolution (%) from the surface to the bottom: 2, 3, 5, 10, 15, 15, 15, 15, 10, 5, 3, 2. This shows that the representation can adequately characterise 3D complex flow structures in Galician estuaries (*e. g.*, Iglesias and Carballo, 2010).

The first step in accurately characterising the 3D hydrodynamics in the Ares-Betanzos estuary is to calibrate and validate model results against field data. With this in mind, current velocity data measured by an ADCP (Acoustic Doppler Current Profiler) deployed at 43°24.30′ N, 8°16.49' W, Fig. 4, during a total period of 35 days (October 15, 2007 to November 19, 2007) is used. The model is simulated during this period by considering the relevant forcing agents and considering an additional spin-up interval of 15 days. Fig. 5 shows the -*x* and *y*-flow components measured by the ADCP (dots) and computed by the model (continuous line) at an intermediate water depth. From a visual inspection, it can be stated that, in general terms, the model reproduces flow measurements with high accuracy, except for certain velocity peaks in the *y*-direction, which are of lower intensity than *x*-direction currents.

These results are corroborated by the statistics comparing modelled and measured velocities, expressed in terms of the correlation coefficient, R, and root mean square error, RMSE. A very good fit is obtained with R = 0.94, RMSE = 0.028 for the velocity component in *x*-direction (*u*), and R = 0.92, RMSE = 0.020 for the velocity component in *y*-direction (*v*).

After being validated, the model is applied to analyse the 3D transient circulation in the Ares-Betanzos estuary throughout a representative period of time, a complete spring-neap tidal cycle, of average circulation. In this regard, it has been shown that the circulation in the Galician estuaries results from the non-linear interaction of various forcings (*e. g.*, Carballo et al., 2009; Iglesias and Carballo, 2010). Nevertheless, during average conditions, tidal action may be considered as the main forcing agent in this coastal area (*e. g.*, Gómez-Gesteira et al., 2002).

Furthermore, the flow intensity caused by river discharges, and leading to barotropic and baroclinic flows, may greatly differ amongst estuaries, with river discharges having larger relative importance compared with the Rías Baixas Region (Duarte et al., 2014). In addition, wind action has been shown to be relevant in the case of specific events (Iglesias and Carballo, 2010), such as upwelling or downwelling periods under winds of a certain intensity. However, they are not representative of average circulation. Thus, for this work, the most representative period for hydrodynamic AR design optimisation is defined as an average complete spring-neap tidal cycle under average discharges of the main river inputs in the coastal area, Fig. 4, average thermohaline conditions and in the absence of winds.

In the present piece of research, the hydrodynamic characterisation focuses on three large zones (Z1, Z2 and Z3), Fig. 4, identified to be of high interest for AR operation based on applying a holistic methodology that considers socioeconomic and environmental aspects, along with the analysis of 2D general hydrodynamic characteristics (Carral et al., 2019). More specifically, the methodology considered the so-called *production factors* grouped into: (i) *excluding factors* related to restrictive uses in the area, (ii) *functional factors* making it possible for the AR to function correctly, e. g., bathymetric, geomorphological and technical aspects, and (iii) *economic factors*, including construction and

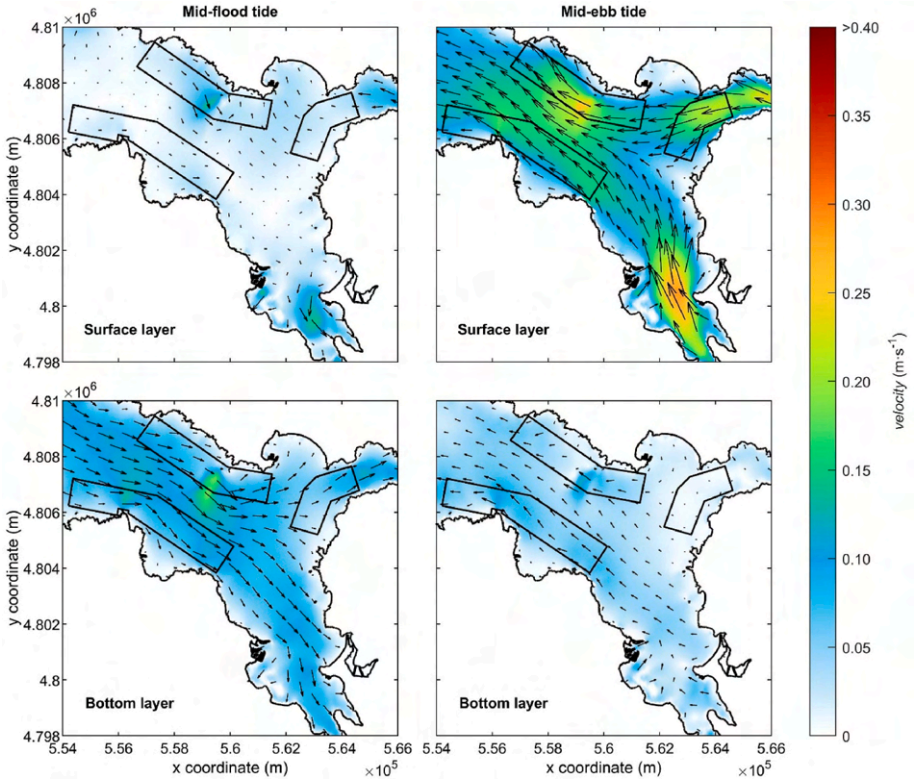

Fig. 7. Transient circulation during mid-flood (left) and mid-ebb tide (right) of a mean neap tide at surface (above) and bottom (below) layers.

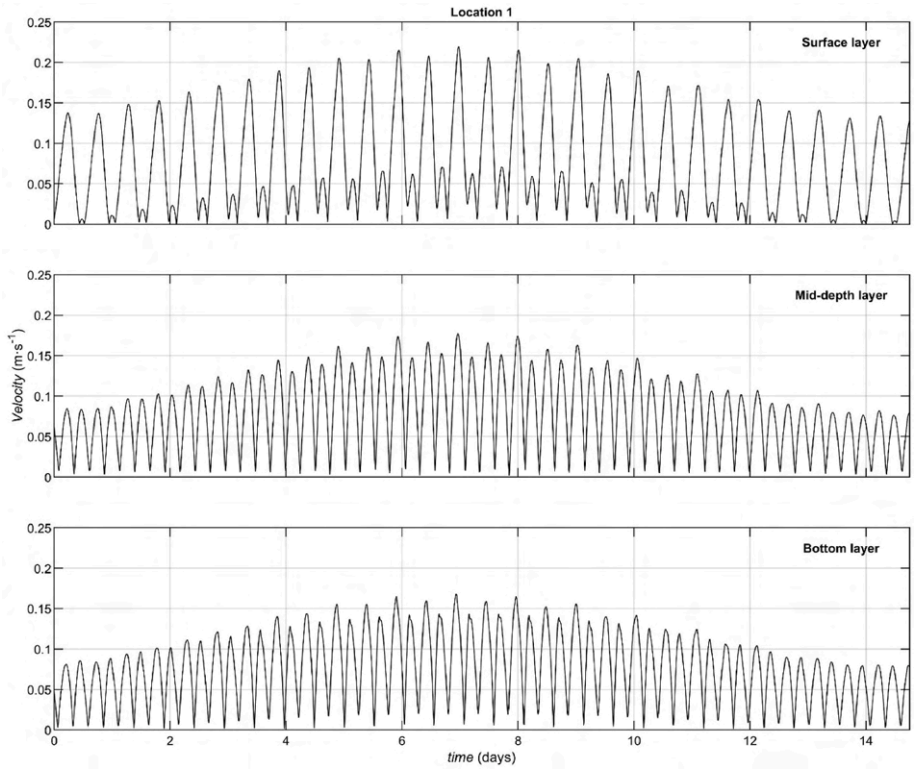

Fig. 8. Velocity time distribution in L1 during a complete spring-neap tidal cycle in surface (upper), intermediate (middle) and bottom (below) layers.

maintenance. Next, as mentioned in Carral et al. (2020), along with 2D general circulation patterns, the flows at specific locations are identified as being representative of each of the delimited zones (L1, L2 and L3, respectively), Fig. 4, were also characterised in terms of vertically averaged flows. Thus, in the present study, these zones and locations of interest were retained for their 3D hydrodynamic analysis.

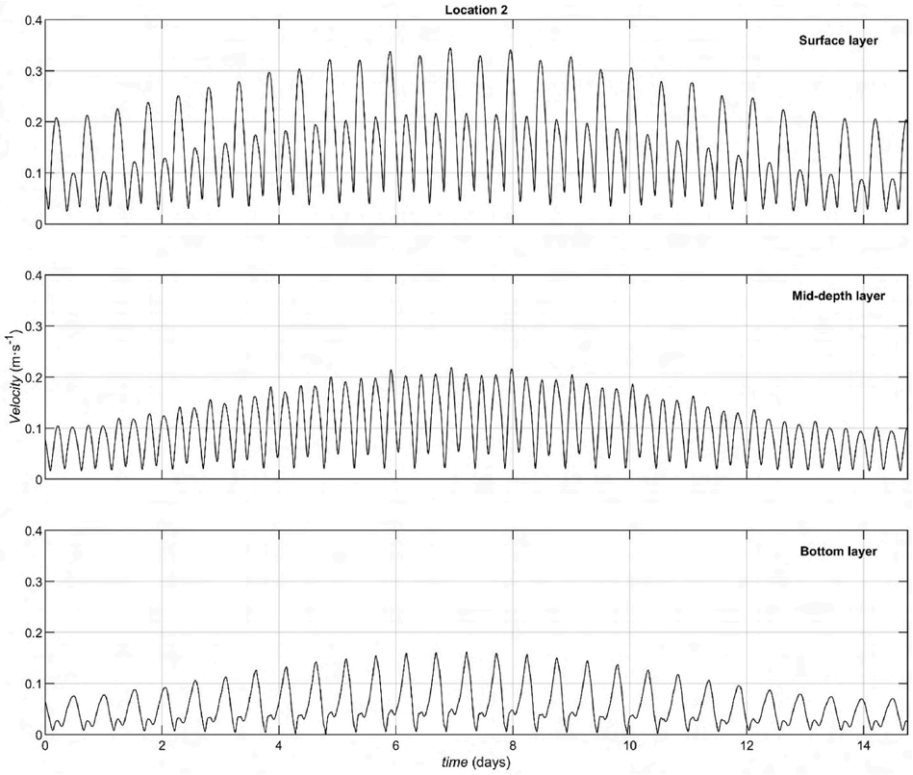

Fig. 9. Velocity time distribution at L2 during a complete spring-neap tidal cycle in surface (upper), intermediate (middle) and bottom (below) layers.

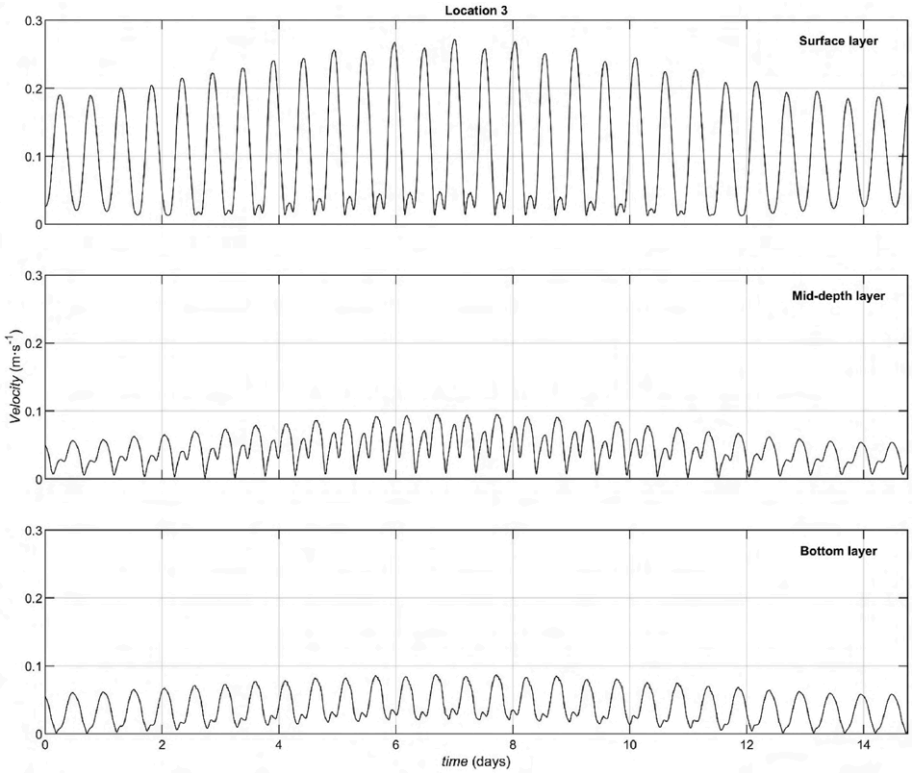

Fig. 10. Velocity time distribution at L3 during a complete spring-neap tidal cycle in the surface (upper), intermediate (middle) and bottom (below) layers.

2.1.2. 3D circulation patterns

The resulting 3D transient circulation is shown in Figs. 6 and 7. In these figures, the flow distribution at mid-flood and mid-ebb tide in surface and bottom layers are plotted for a mean spring tide and a mean neap tide, respectively. Although the general circulation presents striking similitudes between spring and neap tides, the magnitude of the resulting flows significantly differs during both situations and amongst the selected zones of interest. During spring tides, flows greater than

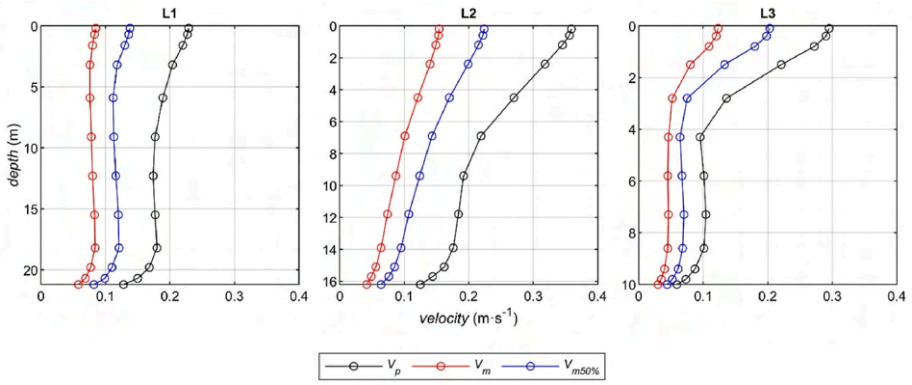

Fig. 11. Results for the 3D site-specific velocity parameters in the representative locations. V_p: peak velocity. V_m: mean velocity. $V_{m50\%}$: mean velocity during the period with flow magnitude above $V_{50\%}$ (threshold velocity exceeded during 50% of the time).

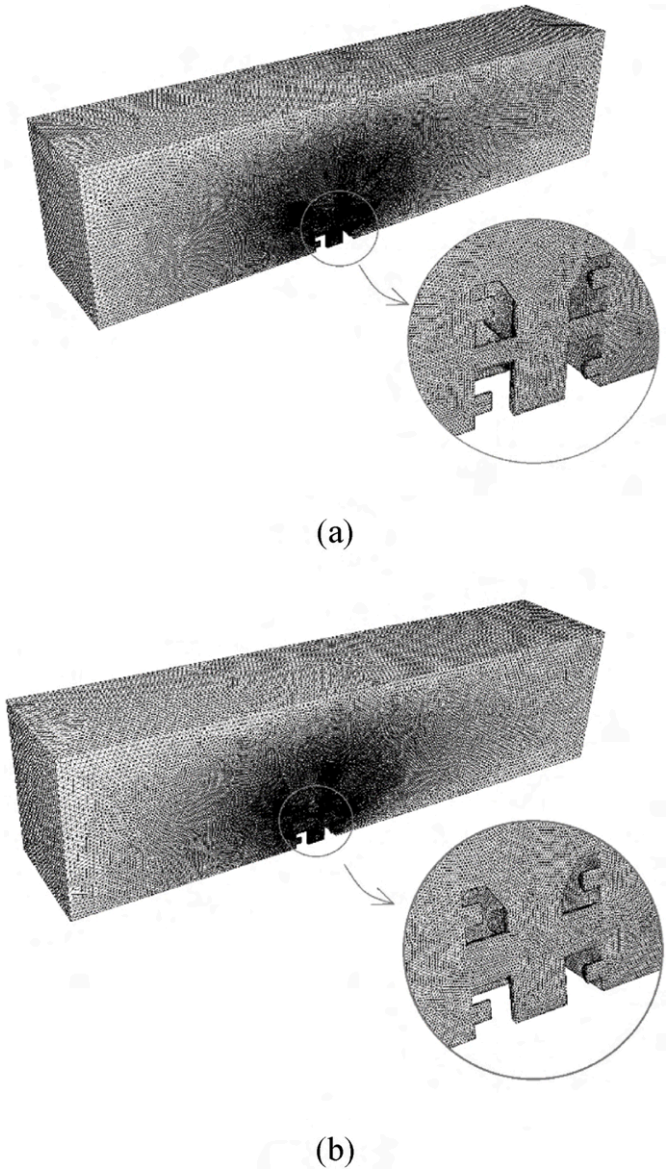

Fig. 12. Computational mesh; (a) orientation A; (b) orientation B.

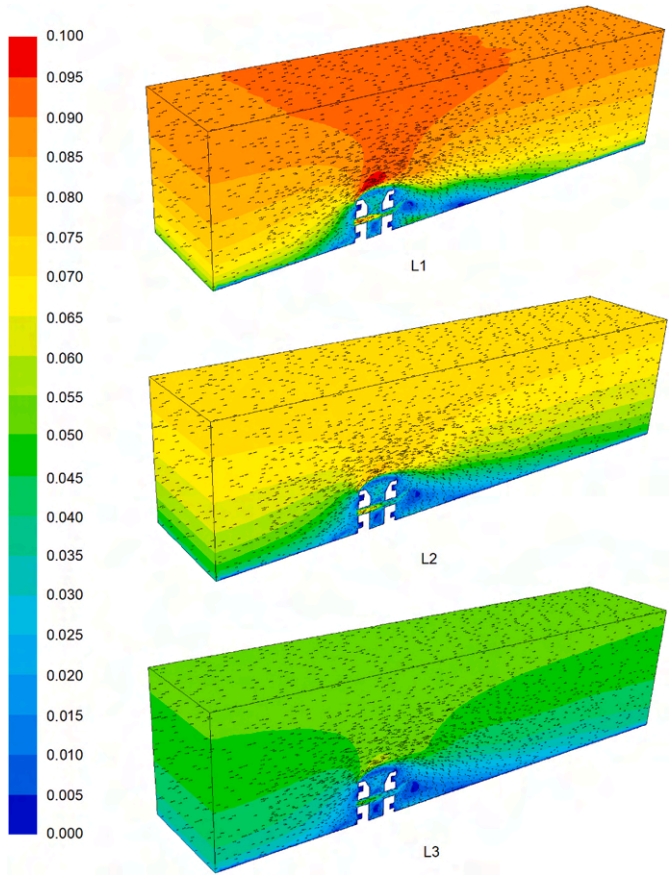

Fig. 13. Velocity field (m·s^{-1}) corresponding to orientation A and current velocities obtained in locations L1, L2 and L3.

0.40 m s^{-1} are attained in Z2 at ebb tide in the surface layers, with extensive areas above 0.30 m s^{-1} in this zone and to a lesser extent in Z1 and Z3 which overall present somewhat lower velocities. During neap tides, flow intensity significantly decreases, not exceeding 0.25–0.30 m s^{-1} in the zones considered.

Also observed is a marked flow asymmetry whose characteristics are more complex than 2D patterns (Carral et al., 2021), which may be explained as follows. In surface layers, ebb velocities are much stronger than flood velocities. In addition to the complex interaction of the tide with the bathymetric configuration, this may be attributed to the presence of barotropic flows generated by the river discharges. These flows tend to reinforce ebb tidal flows and weaken the flood.

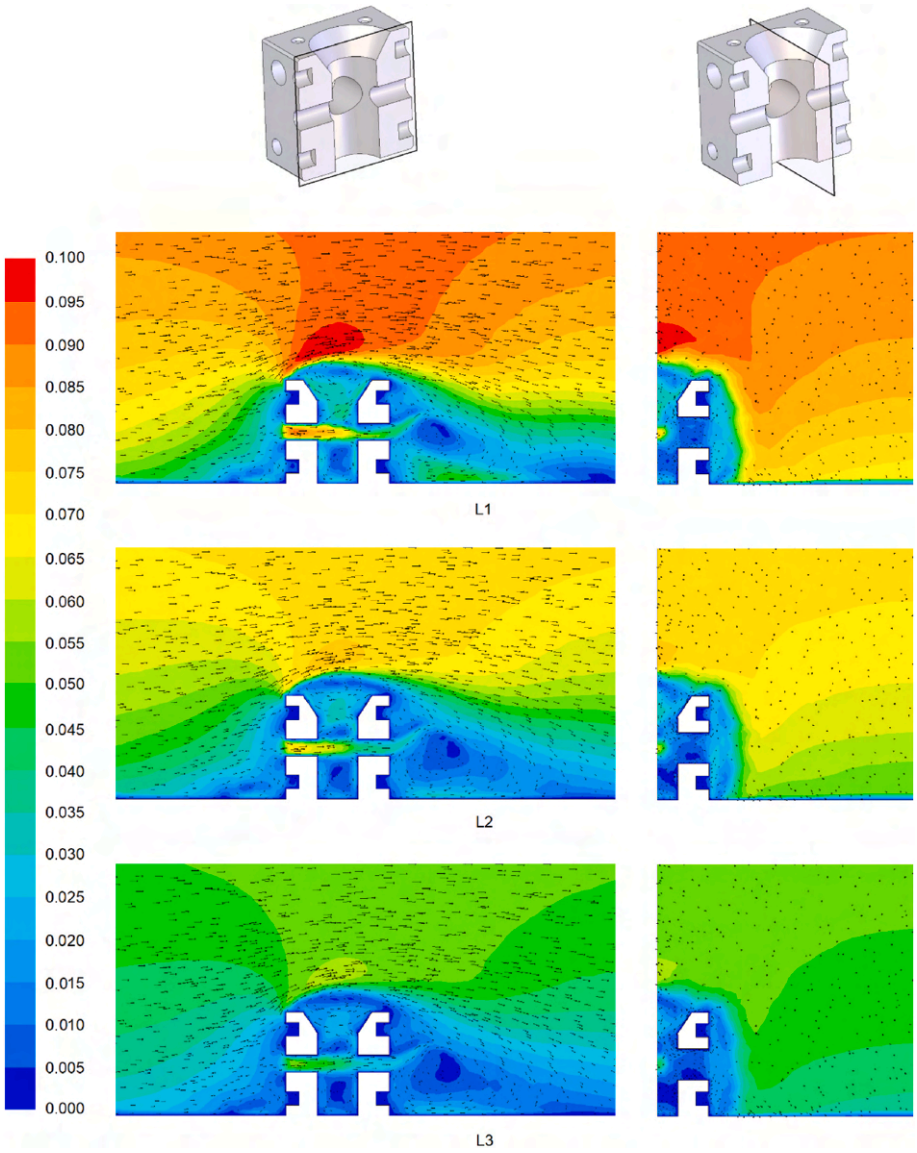

Fig. 14. Detail of the velocity field (m·s^{-1}) around the AR corresponding to orientation A and current velocities obtained in locations L1, L2 and L3. Longitudinal and transversal planes with respect to the current velocity.

This circulation is to some extent compensated in the bottom layers, where a completely different flow structure is present. In effect, during the ebb, bottom-layer flows are much weaker than in surface layers, of about 0.10–0.20 m s^{-1} at spring tides, and 0.05–0.10 m s^{-1} at neap tides, in Z1 and Z2. In Z3, circulation is even weaker. In contrast, during the flood, bottom-layer flows are generally much stronger than in surface layers, of approximately 0.15–0.25 m s^{-1} at spring tides, and 0.10–0.15 m s^{-1} at neap tides, in Z1 and Z2, with again overall weaker velocities in Z3.

A more precise overview of the flows in the locations of interest is shown in Fig. 8, Figs. 9 and 10, which provide the velocity time distribution throughout a complete spring-neap tidal cycle at L1, L2 and L3. Throughout the cycle, a marked time variation of the velocity magnitude is apparent, including inter- and intra-tidal cycle variations. There is also an overall progressive decrease in velocity from the surface to bottom layers. Furthermore, as previously stated, in surface layers, ebb flows are much greater than during the flood, and *vice versa* in bottom layers. Nevertheless, this overall reduction presents different characteristics amongst locations of interest. During the ebb, in L2 and L3, the intensity of the flows in the bottom layers is much lower than in the surface layers. Instead, in L1, the vertical decrease in the velocity intensity is less apparent. Finally, during the flood, in L1 and L3, bottom-layer flows are greater than in the surface, whereas, in L2, surface-layer flows are slightly greater.

To provide a fuller picture of the 3D flow characteristics in the zones and locations of interest, the vertical flow distribution is characterised throughout the entire spring-neap tidal cycle by computing the following site-specific velocity parameters at each vertical grid coordinate. These in turn have been seen to be useful for optimising an AR configuration (Carral et al., 2021): (i) V_p, which represents the peak velocity, (ii) V_m, being the mean velocity, and (iii) $V_{m50\%}$, which stands for the mean velocity of the currents during the period with flow magnitude above $V_{50\%}$, meaning the threshold velocity exceeded during 50% of the time, Fig. 11.

The velocity profiles confirm the previous results. In particular, it is observed that L1 presents similar velocity parameters throughout the water column. However, with slightly higher velocities at the surface and lower velocities close to the sea bottom, the vertical structure is more complex in L2 and L3. In both cases, significant greater velocities are apparent in surface layers, decreasing progressively with depth in L2, and more abruptly in L3, up to a certain depth (of about 4 m), below which there is certain stability in the velocity parameters.

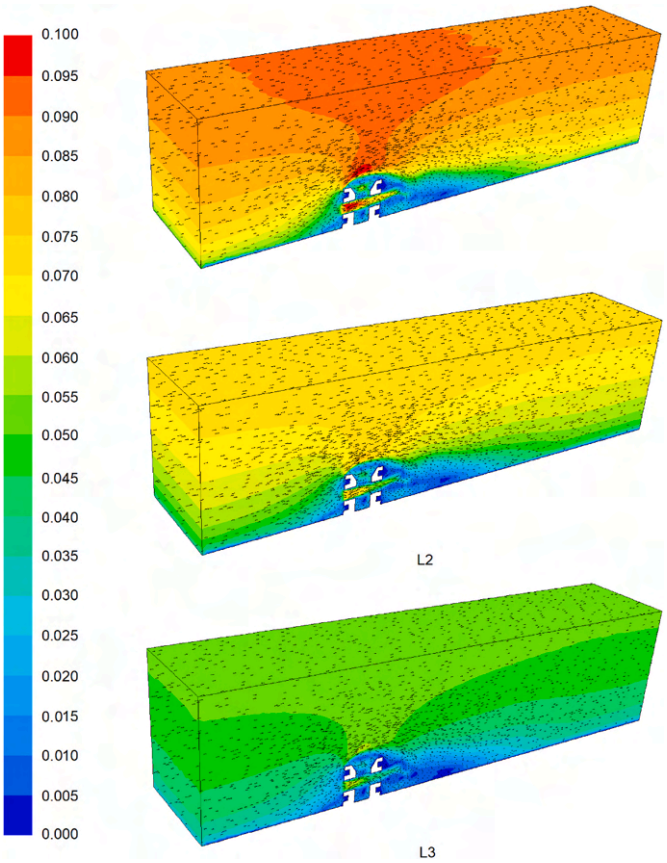

Fig. 15. Velocity field ($m \cdot s^{-1}$) corresponding to orientation B and current velocities obtained in locations L1, L2 and L3.

In the next section, these results are inputs into the HMFDP vsp model. The HMDFP vsp model is based on CFD analyses in which the mean velocities against depth, shown in Fig. 11, are used as boundary conditions. These analyses will be employed to optimise the AR configuration in Section 2.3.

2.2. Hydrodynamic model for food delivery prediction with variable speed profile (HMFDP vsp)

The HMFDP vsp model is based on 3D CFD simulations carried out with the software OpenFOAM. These simulations are based on mass and momentum conservation equations. The k-ε turbulence model is employed. This RANS model is less accurate than other treatments, such as the LES models or DNS. Nevertheless, the validation with experimental results developed in a previous work (Carral et al., 2021) has provided satisfactory accuracy since the differences between the numerical and experimental results were small.

The computational mesh is shown in Fig. 12. Regarding the orientation with respect to the current velocity, two options are analysed.

- Orientation A: 250 mm hole parallel to the current velocity.
- Orientation B: 450 mm hole parallel to the current velocity.

Particularly, Fig. 12 (a) refers to orientation A and Fig. 12 (b) to orientation B. Both domains consist of a 20,000 × 5000 × 4000 m cube. These dimensions are large enough to avoid border effects. The mesh size varies from 0.005 m near the AR surfaces to 0.15 m on the outer surfaces. Several simulations using different mesh sizes were compared to guarantee mesh independence. Regarding boundary conditions, an inlet was imposed on the left part of the domain. As mentioned earlier, the three velocity profiles corresponding to the locations L1, L2 and L3 analysed in the HCM model, Fig. 11, are studied. An outlet was imposed on the right part of the domain. A non-slip boundary condition was applied to the AR surfaces and seabed. The seabed was assumed flat and completely horizontal. By virtue of symmetry, half the geometry of the domain was analysed.

In terms of orientation A, the velocity field provided by this CFD model can be found in Fig. 13. The three locations analysed (L1, L2 and L3) are shown. Fig. 14 details the velocity field around the AR on the longitudinal and transversal planes. Regarding orientation B, the velocity field is shown in Figs. 15 and 16. As can be seen, the AR alters the velocity field and improves the circulation of nutrients. Two important vortices can be obtained for the three locations analysed, which have been illustrated in Fig. 1. First of all, water flow is separated from the seabed and directed upwards, creating an upwelling above the AR. This upwelling is crucial in promoting a vertical circulation of water and thus boosts the transport of nutrients from the seabed. Secondly, another vortex is formed behind the AR. This back vortex is also extremely important in promoting nutrient circulation in this part, which is not exposed to the current velocity. As will be shown in Section 2.3.2, this velocity field indicates that the chosen AR structure is suitable since it guarantees nutrient renewal; this velocity field will be employed to select the most ideal positions for the nest cavities.

2.3. Biological model for colonisation pattern (BMCP)

This section describes how the nest cavity size and shape, as well as position, are determined. These parameters are established according to biological criteria. The process also takes into account the velocity field provided by the HMFDP vsp model described in the previous section.

2.3.1. Nest cavity size and shape (NCSS)

This section establishes a general colonisation pattern and, based on the data obtained, the ideal nest cavity size and shape (NCSS).

The first five years in which ARs could be implemented in the Ares-Betanzos estuary are considered, and the research is based on data about artisanal fishing of commercial benthonic, demersal and pelagic species. The artisanal fishing catches data (Carral et al., 2018; Cartelle Barros et al., 2023) are employed to characterise the main species and develop the BMCP.

Cephalopods, crustaceans and fish are abundant in the Atlantic Iberian Peninsula, especially in the Galician estuaries (Lamas Galdo et al., 2022). They have a high commercial value. Moreover, they play a key role in the biological cycle of many species through a food chain relationship: the different phases of the larval life cycle contribute to the diet of many other species.

These estuaries present two maximum values in phytoplankton, in spring and autumn, and a minimum one in winter. This minimum is caused by two reasons: cold water and high agitation, which suspends the phytoplankton to the photic zone. Phytoplankton is food for zooplankton, zooplankton is food for planktivorous fish and both planktivorous and zooplankton is food for predatory fish, which in turn becomes food for ground fish.

The organisms die and bacteria help them decompose into basic elements as nutrients, deposited on the seabed. At the same time, these deposits can be displaced by water currents, continuously closing the cycle.

Many of the species in the Ares-Betanzos estuary reproduce at the upwelling period of these nutrients. Upwelling facilitates the production of the ecosystem since cold water, rich in nutrients, rises from deep to surface zones and maintains a high concentration of zooplankton (Layman and Allgeier, 2020). This phenomenon is produced from early spring to late autumn. On the other hand, a high concentration of zooplankton can be found along the coast, increasing the availably of nutrients for larvae.

Both nutrient transmission and the presence of hollows play a crucial role as commercial species reproduce in pelagic environments. They

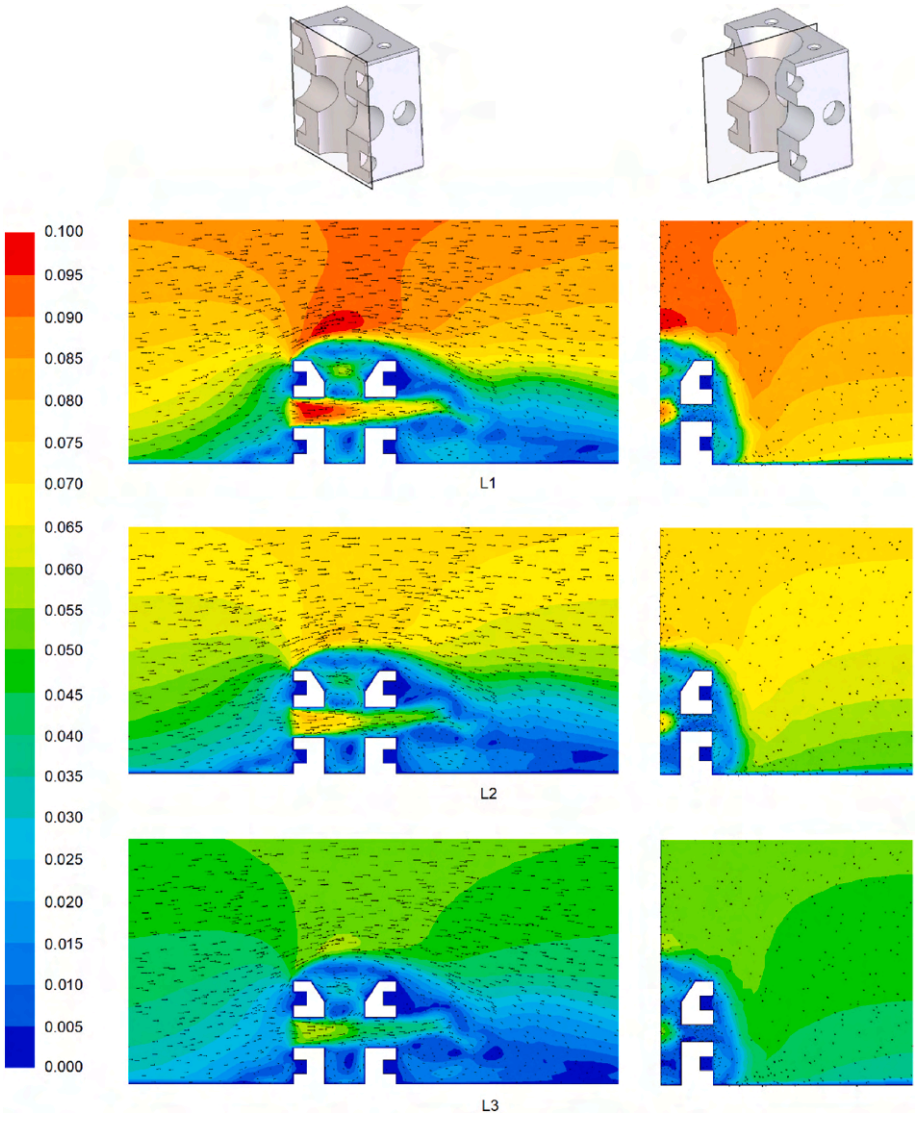

Fig. 16. Detail of the velocity field ($m \cdot s^{-1}$) around the AR corresponding to orientation B and current velocities obtained in locations L1, L2 and L3. Longitudinal and transversal planes with respect to the current velocity.

Table 1
Optimum hole sizes for the species under study.

SPECIES	HOLE SIZE	FUNCTION	HOLLOW	TIME	SOURCE
Cuttlefish (*Sepia officinalis*)	30–40 cm	Reproduction	Open	January–June	Herrera (1998)
Octopi (*Octopus vulgaris*)	30–40 cm	Reproduction	Closed	May–November	Franquet and Brito (1995)
Squid (*Loligo vulgaris*)	30–40 cm	Reproduction	Closed	–	Herrera (1998); Franquet and Brito (1995)
Lobsters *(Paliinuros elephas*)	Less than 25 cm	Habitat	Closed	–	Spanier (2000)
Other crustaceans	Less than 20 cm	Habitat	Closed	–	Herrera (1998)

take part in migratory movements in search of a suitable place and moment for laying. Other species reproduce in benthonic environments and need particular structures for laying. The main causes of mortality are hunger and predation. Hunger occurs when larvae lack nutrients and predation may happen when larvae do not have a haven in which to hide. In this sense, ARs provide both nutrients and havens (Fossheim et al., 2006).

The nest cavity size and shapes (NCSS) are established according to the species that may colonise the AR. The analysed region has many benthonic and pelagic species. The species that have experienced the most significant reduction in the last ten years are cephalopods and crustaceans, with stock reductions higher than 50% (Carral et al., 2018). Thus, a review with an analysis of the species and the optimal hole sizes was carried out in previous works (Carral et al., 2022; Lamas Galdo et al., 2022; Cartelle et al., 2023). Table 1 summarises the most significant species that may colonise the AR and the corresponding optimum hole size. Taking into account this review and the fact that the cylindrical shape facilitates the manufacturing process (Lamas Galdo et al., 2022), nest cavities that are cylindrical in shape are proposed. Regarding the size of the nest cavities, the 200 and 300 mm diameters mentioned previously are selected, as shown in Table 1.

2.3.2. *Nest cavity position (NCP)*

As mentioned earlier, the CFD model described in Section 2.2

Table 2
Value of *NM* (nutrient modification) and *HM* (habitat modification) to allocate nest cavities.

VELOCITY (LOCATION) - ORIENTATION	UPWELLING REGION ($Effect_{upwelling}$)	BACK EDDY REGION ($Effect_{back\ eddy}$)	INTERIOR CAVITY ($Effect_{interior\ hole}$)	NUTRIENT MODIFICATION (*NM*)	LOCATION OF NEST CAVITIES -(HM_{front} and HM_{back})	*LOCATION OF NEST CAVITIES -($HM_{lateral}$)*	HABITAT MODIFICATION (*HM*)
High velocity (L1) – Orientation A	Optimal (3)	Optimal (3)	Optimal (3)	Optimal (9)	High, mid and low positions Optimal (3) + (3)	*High, mid and low positions* *Optimal (3)*	Optimal (9)
Medium velocity (L2) – Orientation B	Optimal (3)	Optimal (3)	Sufficient (2)	Optimal (8)	High, mid and low positions Optimal (3) + (3)	High, mid and low positions Optimal (3)	Optimal (9)
Low velocity (L3) – Orientation A	Optimal (3)	Optimal (3)	Sufficient (2)	Optimal (8)	High, mid and low positions Optimal (3) + (3)	High, mid and low positions Optimal (3)	Optimal (9)
High velocity (L1) – Orientation B	Sufficient (2)	Sufficient (2)	Optimal (3)	Sufficient (7)	High and mid positions at the front face. Mid and low positions at the back face Sufficient (2) + (2)	High, mid and low positions Optimal (3)	Sufficient (7)
Medium velocity (L2) – Orientation B	Sufficient (2)	Sufficient (2)	Optimal (3)	Sufficient (7)	High and mid positions at the front face. Mid and low positions at the back face Sufficient (2) + (2)	High, mid and low positions Optimal (3)	Sufficient (7)
Low velocity (L3) – Orientation B	Sufficient (2)	Sufficient (2)	Optimal (3)	Sufficient (7)	High and mid positions at the front face. Mid and low positions at the back face Sufficient (2) + (2)	High, mid and low positions Optimal (3)	Sufficient (7)

corroborated the upwelling and back eddy regions illustrated in Fig. 1, essential for improving the delivery of nutrients. In this section, the results of the CFD model are also employed to determine the most suitable position for the nest cavities. To this end, an index is established, Eq. (5), through two intermediate sub-indices: *NM* (nutrient modification) and *HM* (habitat modification). Each of these sub-indices represents the possibilities of the AR compensating deficiencies in the ecosystem.

$$AR_{nest\ cavity\ position\ index} = NM + HM \tag{5}$$

To modify nutrient circulation, the hydrodynamic effect is produced by three factors: upwelling, back eddy and the interior hole, Eq (6). The third one represents circulation along the interior hole.

$$NM = Effect_{upwelling} + Effect_{back\ eddy} + Effect_{interior\ hole} \tag{6}$$

The term *HM* is related to the number of cavities adapted to the species in the region, Eq. (7).

$$HM = HM_{front} + HM_{back} + HM_{lateral} \tag{7}$$

The term, HM_i, depends on the number of cavities adapted to the species in the region, on each face "*i*" Eq. (8)

$$HM_i = number\ of\ cavities\ (size, type\ and\ number) \tag{8}$$

In this way, the term HM_i evaluates the total number of nest cavities of diameter *l* created, Eq. (9).

$$HM_i = \sum_l Nest\ cavities\ number\ l_i \cdot Surface_{Nest\ cavities\ l} \tag{9}$$

The cases analysed are summarised in Table 2. The two orientations analysed (orientation A and orientation B) are shown in this table and three current velocities corresponding to the locations studied: high current velocity at location L1, medium current velocity at location L2 and low current velocity at location L3. Values between 1 and 3 are assigned to $Effect_{upwelling}$, $Effect_{back\ eddy}$,$Effect_{interior\ cavity}$, HM_{front}, HM_{back}, and $HM_{lateral}$, where 1 represents a bad result, 2 a sufficient result, and 3 an optimal result. This leads to *NM* and *HM* values from 3 to 9. *HM* values are also assigned using a scale with as 9 the maximum result. These indices are thus based on a discontinuous scale instead of a continuous one, in the aim of establishing a comparative metric. A discontinuous scale was stablished in order to characterise the results into clear and distinct categories with no values in between the qualitative information because the categories have no numerical relationship to each other. In other words, several possibilities are compared and three categories are established (bad, sufficient and optimal): these are represented by discontinuous values (1, 2 and 3). This perspective provides an interpretable representation of the complex process that takes place. By discretising these values, it is possible to communicate the information more effectively and carry out the decision-making process. By assigning different values to different levels, it is easy to compare them and determine the most appropriate option.

The results are shown in Table 2. As can be seen in this table, orientation A provides adequate nutrient delivery along the entire AR, and thus nest cavities can be placed at high, mid and low positions. On the other hand, orientation B provides poorer upwelling and back eddy regions; high and mid positions are therefore recommended for the front face and mid and low positions for the back face. The current velocity is perpendicular to the lateral faces, and adequate circulation is obtained along them. According to this, high, mid and low positions are appropriate for nest cavities at the lateral faces.

Regarding habitat modification (*HM*), orientation A is more appropriate because more nest cavities can be allocated along the entire surface made up of the AR faces. Nevertheless, in orientation B, low positions at the front face and high positions at the back face are less efficient.

3. Conclusions

Estuaries stand out as promising sites for AR operation. These coastal bodies may present a complex 3D transient flow structure under average conditions, which has to be accurately characterised to obtain a suitable design and configuration for the AR group deployed at the sea bottom. This is the case of a large part of estuaries without large tidal ranges, where a 3D flow structure can be present under average conditions, as a result of the influence of the river discharges on the hydrodynamics. Thus, for an appropriate performance of an AR group, the 3D flow structure of the coastal area of interest for AR operation must be thoroughly characterised and used for AR optimisation. To this end, in this study, the state-of-the-art open-source code DELFT3D FLOW is validated

and applied to the Ares-Betanzos estuary (NW Spain), where the installation of an AR group has been recently proposed. A complete average spring-neap tidal cycle under average conditions, including river discharges and thermohaline conditions, is retained as the most representative period for AR design. The hydrodynamic characterisation focuses on three zones (Z1, Z2 and Z3), and in particular, at their representative locations (L1, L2 and L3, respectively), identified to be of interest for AR operation. The general circulation patterns present strong similarities throughout the spring-neap tidal cycle. However, the magnitude of the resulting flows widely differs, both in time and amongst the selected zones and locations of interest. In view of the great variability in the magnitude of the currents amongst the zones and locations of interest, the vertical flow distribution is thoroughly characterized throughout the complete spring-neap tidal cycle by computing different velocity parameters at each vertical grid coordinate: V_p, V_m, and $V_{m50\%}$, which are retained for CFD optimisation.

The results provided by the CFD model are used to apply the indicator $AR_{nest\ cavity\ position}$ to two orientations: orientation A and orientation B. This index takes into account the modification of nutrients and habitats. In turn, nutrient modification considers three aspects: upwelling, back eddy and the interior hole. The last one represents circulation along the interior hole. The result is that orientation A leads to suitable nutrient delivery to the whole AR, and thus nest cavities can be located in low, mid and high positions. Nevertheless, orientation B provides sufficient nutrient delivery to high and mid positions at the front face and mid and low positions at the back face. The nutrient delivery at lateral faces is sufficient in both orientations A and B. Regarding habitat modification, orientation A is more appropriate because more nest cavities can be allocated along the entire surface of the AR faces. Nevertheless, with orientation B, low positions at the front face and high positions at the back face are less efficient.

Funding

This research was funded by Xunta de Galicia through the project CN-10MMA003CT. This study was also funded through the collaboration agreement between the Xunta de Galicia (Convenio de colaboración entre a Xunta de Galicia, a Universidade da Coruña e a Fundación da Universidade da Coruña para dar continuidade ao Proxecto de investigación de arrecife artificial – PROARR), Universidade da Coruña and the Universidade da Coruña Foundation (FUAC) to give continuity to the previous project.

Declaration of competing interest

The authors declare that they have no known competing financial interests or personal relationships that could have appeared to influence the work reported in this paper.

Data availability

The authors do not have permission to share data.

References

Bacher, C., Grant, J., Hawkins, A.J.S., Fang, J., Zhu, M., Besnard, M., 2003. Modelling the effect of food depletion on scallop growth in Sungo Bay (China). Aquat. Living Resour. 16, 10–24. https://doi.org/10.1016/S0990-7440(03)00003-2.

Bohnsack, J.A., Sutherland, D.L., 1985. Artificial reef research: a review with recommendations for future priorities. Bull. Mar. Sci. 37, 11–39.

Camba, C., Mier, J.L., Carral, L., Lamas, M.I., Álvarez, J.C., Díaz-Díaz, A.M., Tarrío-Saavedra, J., 2021. Erosive degradation study of concrete augmented by mussel shells for marine construction. J. Mar. Sci. Technol. 9, 1087, 2077-1312/9/10/1087.

Carballo, R., Iglesias, G., Castro, A., 2009. Residual circulation in the Ría de Muros (NW Spain): a 3D numerical model study. J. Mar. Syst. 75 https://doi.org/10.1016/j.jmarsys.2008.08.004, 130-130.

Carral, L., Rodriguez-Guerreiro, M., Tarrio-Saavedra, J., Alvarez-Feal, J.C., Fraguela Formoso, J., 2018. Social interest in developing a Green modular artificial reef structure in concrete for the ecosystems of the Galician rías. J. Clean. Prod. 172, 1881–1898. https://doi.org/10.1016/j.oceaneng.2016.06.030.

Carral, L., Rodríguez-Guerreiro, M.J., Vargas, A., Arean, N., Carballo, R., Alvarez-Feal, C., 2019. Methodology for positioning a group of green artificial reef based on a database management system, applied in the Estuary of Ares-Betanzos (NW Iberian Peninsula). J. Clean. Prod. 233, 1047–1060. https://10.1016/j.jclepro.2019.06.092.

Carral, L., Camba Fabal, C., Lamas Galdo, M.I., Rodriguez-Guerreiro, M.J., Cartelle Barros, J.J., 2020. Assessment of the materials employed in green artificial reefs for the Galician estuaries in terms of circular economy. Int. J. Environ. Res. Publ. Health 17, 8850. https://doi.org/10.3390/ijerph17238850.

Carral, L., Lamas–Galdo, M.I., Rodríguez-Guerreiro, M.J., Vargas, A., Álvarez-Feal, C., López, I., Carballo, R., 2021. Configuration methodology for a green variety reef system (AR group) based on hydrodynamic criteria – application to the Ría de Ares-Betanzos. Estuarine. Coastal and Shelf Science 252, 107301. https://doi.org/10.1016/j.ecss.2021.107301.

Carral, L., Lamas, M.I., Cartelle Barros, J.J., López, I., Carballo, R., 2022. Proposed conceptual framework to design artificial reefs based on particular ecosystem ecology traits. Biology 11, 680. https://doi.org/10.3390/biology11050680.

Carral, L., Lamas-Galdo, M.I., Mier Buenhombre, J.L., Cartelle Barros, J.J., Naya, S., Tarrio-Saavedra, J., 2023. Application of residuals from purification of bivalve molluscs in Galician to facilitate marine ecosystem resiliency through artificial reefs with shells – one generation. Sci. Total Environ. 856, 159095 https://doi.org/10.1016/j.scitotenv.2022.159095.

Cartelle Barros, J.J., Lamas Galdo, M.I., Rodríguez Guerreiro, M.J., Carral Couce, L., 2023. Biological and hydrodynamic aspects for the design of artificial reef modules for cephalopod molluscs in the Ares-Betanzos estuary. J. Mar. Sci. Eng. 11, 1365. https://doi.org/10.3390/jmse11071365.

Collins, K.J., Jensen, A.C., Lockwood, A.P.M., 1990. Fishery enhancement reef building exercise. Chem. Ecol. 4, 179–187. https://doi.org/10.1080/02757549008035232.

Deltares, 2010. In: Deltares (Ed.), Delft3D-Flow. User Manual. 2010. Delft, The Netherlands.

Duarte, P., Alvarez-Salgado, X.A., Fernández-Reiriz, M.J., Piedracoba, S., Labarta, U., 2014. A modeling study on the hydrodynamics of a coastal embayment occupied by mussel farms (Ría de Ares-Betanzos, NW Iberian Peninsula). Estuarine. Coastal & Shelf Science 147, 42–55. https://doi.org/10.1016/j.ecss.2014.05.021.

Fossheim, M., Tande, K.S., Semenova, T., Timonin, A., 2006. Capelin larvae (Mallotus villosus) and community structure of zooplankton off the coast of northern Norway. J. Plankton Res. 28, 585–595. https://doi.org/10.1093/plankt/fbi143.

Franquet, F., Brito, A., 1995. Especies de interés pesquero de Canarias. Consejería de Pesca y Transportes del Gobierno de Canarias. St. Cruz Tenerife.

Godoy, E., Almeida, T., Zalmon, I., 2002. Fish assemblages and environmental variables on an artificial reef north of Rio de Janeiro, Brazil. ICES J. Mar. Sci. 59, S138–S143. https://doi.org/10.1006/jmsc.2002.1190.

Gómez-Gesteira, M., de Castro, M., Prego, R., Martins, F., 2002. Influence of the Barrie de la Maza dock on the circulation patterns of the Ría of A Coruña (NW-Spain). Sci. Mar. 66, 337–346.

Haro, A., Castro-Santos, T., Noreika, J., Odeh, M., 2004. Swimming performance of upstream migrant fishes in open-channel flow: a new approach to predicting passage through velocity barriers. Can. J. Fish. Aquat. Sci. 61, 1590–1601. https://doi.org/10.1139/f04-093.

Herrera, R., 1998. Dinámica de las comunidades bentónicas de los arrecifes artificiales de Arguineguín (Gran Canaria) y Lanzarote. Ph. D.

Huang, Y.D., Fu, D.F., He, W.R., 2014. Three-dimensional numerical simulation on influence of cut-opening ratio of artificial reef on flow effect. J. Water Resour. Water Eng. 25, 39–43.

Iglesias, G., Carballo, R., 2010. Effects of high winds on the circulation of the using a mixed open boundary condition: the Ría de Muros, Spain. Environ. Model. Software 25, 455–466. https://doi.org/10.1016/j.envsoft.2009.10.013.

Kim, D., Woo, J., Yoon, H.S., Na, W.B., 2016. Efficiency, tranquility and stability indices to evaluate performance in the artificial reef wake region. Ocean Eng 122, 253–261. https://doi.org/10.1016/j.oceaneng.2016.06.030.

Lamas Galdo, M.I., Rodriguez Guerreiro, M.J., Lamas Vigo, J., Ameneiros Rodríguez, I., Veira Lorenzo, R., Carral Couce, J.C., Carral, L., 2022. Definition of an artificial reef unit through hydrodynamic and structural (CFD and FEM) models, application to the Ares-Betanzos Estuary. Journal of the Maritime Science and Engineering 10, 230. https://doi.org/10.3390/jmse10020230.

Lan, C.H., Chen, C.C., Hsui, C.Y., 2004. An approach to design spatial configuration of artificial reef ecosystem. Ecol. Eng. 22, 217–226. https://doi.org/10.1016/j.ecoleng.2004.04.004.

Layman, C.A., Allgeier, J.E., 2020. An ecosystem ecology perspective on artificial reef production. J. Appl. Ecol. 57, 2139–2148. https://doi.org/10.1111/1365-2664.13748.

Liu, Y., Zhao, Y.P., Cui, Y., Dong, G.H., 2012. Experimental study of the flow field around cube artificial reef. Ocean Eng 30, 103–108.

Liu, T.L., Su, D.T., 2013. Numerical analysis of the influence of reef arrangements on artificial reef flow fields. Ocean Eng 74, 81–89. https://doi.org/10.1016/j.oceaneng.2013.09.006.

London Convention and Protocol/UNEP, 2009. London Convention and Protocol/UNEP Guidelines for the Placement of Artificial Reefs. London, UK.

Lotze, H.K., Guest, H., O'Leary, J., Tuda, A., 2018. Public perceptions of marine threats and protection from around the world. Ocean Coast Manag. 152, 14–22. https://doi.org/10.1016/j.ocecoaman.2017.11.004.

Oudon, B., Belaidi, C., Salaun, J., Coutu, A., 2022. Xflow modelling for investigation of fluid structure interaction of artificial reef: application to burial effect. Computer Aided Chemical Engineering 51, 529–534. https://doi.org/10.1016/B978-0-323-95879-0.50089-8.

Pickering, H., Whitmarsh, D., 1997. Artificial reefs and fisheries exploitation: a review of the "attraction versus production" debate, the influence of design and its significance for policy. Fish. Res. 31, 39–59. https://doi.org/10.1016/S0165-7836(97)00019-2.

Rickels, W., Dovern, J., Quaas, M., 2016. Beyond fisheries: common-pool resource problems in oceanic resources and services. Global Environ. Change 40, 37–49. https://doi.org/10.1016/j.gloenvcha.2016.06.013.

Rodríguez-Guerreiro, M.J., Álvarez-Feal, J.C., Fraguela-Formoso, J.A., Castro-Santos, L., Carral-Couce, L., 2019. Application of a general pattern of colonization of a 'verde-PROARR' artificial reef in the Ría de Ares-Betanzos (Spain). In: Proceedings of the VI International Ship Design & Naval Engineering Congress (CIDIN) and XXVI Pan-American Congress of Naval Engineering. Maritime Transportation and Port Engineering—COPINAVAL, Cartagena de Indias, Colombia.

Spanier, E., 2000. Artificial reefs off the mediterranean coast of Israel. Artificial Reefs in European Seas 1–19. Dordrecht: Springer Netherlands.

Wang, G., Wan, R., Wang, X., Zhao, F., Lan, X., Cheng, H., Tang, W., Guan, Q., 2018. Study on the influence of cut-opening ratio, cut-opening shape, and cut-opening number on the flow field of a cubic artificial reef. Ocean Engineering 162, 341–352. https://doi.org/10.1016/j.oceaneng.2018.05.007.

Yoon, H.S., Kim, D., Na, W.B., 2016. Estimation of effective useable and burial volumes of artificial reefs and the prediction of cost-effective management. Ocean Coast Manag. 120, 135–147. https://doi.org/10.1016/j.ocecoaman.2015.12.007.

Zheng, Y., Kuang, C., Zhang, J., Tu, J., Chen, K., Liu, X., 2022. Current and turbulence characteristics of perforated box-type artificial reefs in a constant water depth. Ocean Engineering 244, 110359. https://doi.org/10.1016/j.oceaneng.2021.110359.